Particle resolved direct numerical simulation of a liquid-solid fluidized bed: Comparison with experimental data

A. Ozel, J.C. Brändle de Motta, Micheline Abbas, Pascal Fede, Olivier C Masbernat, Stéphane Vincent, Jean-Luc Estivalèzes, Olivier Simonin

Particle Resolved Direct Numerical Simulation of a Liquid-Solid Fluidized Bed: Comparison with Experimental Data

A. Ozel[a], J. C. Brändle de Motta[a], M. Abbas[b], P. Fede[a], O. Masbernat[b,*], S. Vincent[c,d], J.-L. Estivalezes[a], O. Simonin[a]

[a] *Institut de Mécanique des Fluides de Toulouse (IMFT), Université de Toulouse, CNRS, INPT, UPS, Toulouse, France*
[b] *Laboratoire de Génie Chimique, Université de Toulouse, CNRS, INPT, UPS, Toulouse, France*
[c] *Université Paris-Est Marne-La-Vallée, UMR 8208, Laboratoire de Modélisation et Simulation Multi Echelle (MSME), F-77454 Marne-La-Valle*
[d] *Université de Bordeaux; Institut Polytechnique de Bordeaux (IPB), Institut de Mécanique et Ingénierie (I2M); F-33000 Bordeaux*

Abstract

Particle-resolved direct numerical simulations of a 3-D liquid-solid fluidized bed experimentally investigated by Aguilar-Corona (2008) have been performed at different fluidization velocities (corresponding to a range of bed solid volume fraction between 0.1 and 0.4). Particle Reynolds number and Stokes number are $O(100)$ and $O(10)$, respectively. In these simulations, the flow is solved by a one-fluid formulation of the incompressible Navier-Stokes equations, where the pressure-velocity coupling is provided by an algebraic augmented Lagrangian method. The particle presence is modeled by an implicit penalty fictitious domain method and the particle-to-wall and particle-to-particle interactions are taken into account by a linear spring-dashpot model and a sub-grid scale lubrication force.In this paper, we compare the statistical quantities computed from numerical results with the experimental data obtained with 3-D trajectography and High Frequency PIV. Fluidization law predicted by the numerical simulations is in very good agrement with the experimental curve and the main features of trajectories and Lagrangian velocity signal of the particles are well

*Corresponding author

reproduced by the simulations. The evolution of particle and flow velocity variances as a function of bed solid volume fraction is also well captured by the simulations. In particular, the numerical simulations predict the right level of anisotropy of the dispersed phase fluctuations and its independence of bed solid volume fraction. They also confirm the high value of the ratio between the fluid and the particle phase fluctuating kinetic energy. A quick analysis suggests that the fluid velocity fluctuations are mainly driven by fluid-particle wake interactions (pseudo-turbulence) whereas the particle velocity fluctuations derive essentially from the large scale flow motion (recirculation). Lagrangian autocorrelation function of particle fluctuating velocity exhibits large-scale oscillations, which are not observed in the corresponding experimental curves, a difference probably due to a statistical averaging effect. Evolution as a function of the bed solid volume fraction and the collision frequency based upon transverse component of particle kinetic energy correctly matches the experimental trend and is well fitted by a theoretical expression derived from Kinetic Theory of Granular Flows.
Keywords: Particle-resolved DNS, liquid-solid fluidized bed, particle and fluid agitation,

---

1. Introduction

Liquid fluidization is used in various industrial application involving biochemical, catalytic reactions and crystallization processes. The flow in a liquid fluidized bed lies within an intermediate regime between the settling of particles controlled by the hydrodynamic interactions and the rapid granular flow controlled by the collisions between particles, where the particle Reynolds number is in a range of $O(100)$ and the particle Stokes number is in a range of $O(10)$, both based on particle settling velocity. In this sense, liquid fluidization is a challenging problem for two-phase modeling. For practical applications, two-phase continuum models are generally used to carry out numerical simulations, based upon two-fluid or statistical models (Gevrin et al., 2008, Zhang et al.,

2013). However, modeling of liquid-solid fluidization is still an open research topic and multi-scale modeling developments are still needed to correctly predict inter-particle and particle-fluid interactions. One major issue is to predict the right level of particulate and carrying flow phase fluctuations as a function of bed solid phase fraction (or fluidization velocity).

Resolved particle direct numerical simulations of particulate flows has been developing last two decades (see the review of Tenetti and Subramanian (2014)). These simulations can provide the particulate phase fluctuation characteristics in order to develop appropriate two-phase continuum models. Many of particle resolved simulations have been carried out on fixed structured grids to take advantage of parallelization and avoid the complexity of mesh reconstruction.

Pan et al. (2002) carried out resolved simulations of fluidization of 1204 finite size spheres in a 2-D bed using the method of distributed Lagrange multipliers and as simulation results, the fluidization velocity versus fluid fraction was found to be a power law which exponent well compared with that predicted by the correlation of Richardson and Zaki (1954). Zhang et al. (2006) performed a 3-D fully resolved simulation of 1024 particles settling under gravity in a periodic domain accounting for elastic collisions of particles. Their method is based on a linearization of Navier-Stokes equations in the vicinity of particle interface (Zhang and Prosperetti (2005)). In their study, Particle Reynolds number and solid volume fraction were respectively 10% and 13%. They have shown that the settling velocity was matching Richardson & Zaki (1954) correlation and evidenced the relation between the velocity fluctuations and particles microstructuration.

Using a Lattice Boltzmann Method to solve the interstitial flow and an equation of motion accounting for lubrication and collisions between particles, Derksen and Sundaresan (2007) have simulated in limited size domains the propagation of concentration waves in liquid-solid fluidized beds with large bed solid fraction (close to maximum packing) and particle Reynolds number of order of $O(10)$. Their results were in qualitative agreement with an experimental study of Duru and Guazzelli (2002). Based on the same method, Derksen (2014)

performed the simulation of the mixing of a passive scalar in a fluidized bed with periodical boundaries in a wide range of bed solid volume fraction (0.2-0.5) and particle Reynolds numbers of order 10. Derksen's results first show a good agreement with Richardson & Zaki (1954) exponent dependence with Reynolds number. Interestingly, Derksen (2014) showed that the diffusion of the passive scalar in the bed is similar to the auto-diffusion of particles, scaling of which is close to what was experimentally observed in sedimentation by Nicolai et al. (1995).

Uhlmann (2005) developed an Immersed Boundary Method to simulate the sedimentation of 1000 spherical finite particles at high Reynolds number (400) and highly dilute limit, but no quantitative comparison with existing data was provided. More recently, Uhlmann and Dušek (2014) evaluated the accuracy of their method as a function of the spatial resolution (number of meshes per particle diameter) for the case of a single sphere settling in an infinite stagnant fluid, in a wide range of Reynolds and Archimedes (or Galileo) numbers. The higher the latter number, the higher spatial resolution is required, up to 48 mesh points per particle diameter at high Galileo number. Then Chouippe and Uhlmann (2015) used this method to study turbulent particle settling in a channel.

Corre et al. (2010) used a fictitious domain approach to perform particle-resolved simulations of the liquid-fluidized bed experimentally studied by Aguilar-Corona (2008). Instantaneous and averaged flow characteristics of the fluidized bed were qualitatively in good agreement with experimental trends. Since then, this method was improved and has been applied in the present study with a higher level of accuracy (Vincent et al. (2014)). The numerical technique is a four-way coupling method, based on a one-fluid formulation of the incompressible Navier-Stokes equations solved on a structured Cartesian grid. The resolved-scale particles are modeled by an Implicit Tensorial Penalty Fictitious Domain Method (ITPM). They are tracked by using a hybrid Eulerian-Lagrangian Volume of Fluid approach, which accounts for collisions and lubrication effects.

This study has two scopes. The first one is to evaluate the effective ability of ITPM to predict two-phase flow behaviour by performing particle resolved simulations of a liquid-solid fluidized bed involving finite size particles, with large particle Reynolds and moderate Stokes numbers. The second one is to analyse velocity fluctuations of both phases in this regime. The bed geometry, particle size and number and flow parameters used in these simulations are the same as in Aguilar's experiments, allowing a direct quantitative comparison between experiments and numerical data.

The paper is structured as follows: Flow parameters and numerical model (detailed in other references) are briefly presented in sections 2 and 3 respectively. Statistical quantities (as defined in appendix A) computed from the numerical results are compared with experimental data obtained by Aguilar Corona with same flow parameters and geometry. Fluidization law and particle velocity fluctuations predicted by the simulations are also compared in section 4.

2. Flow parameters

Flow parameters chosen for the simulation of the fluidized bed are taken from the experimental study of Aguilar-Corona (2008) in a cylindrical column of $8\,cm$ inner diameter. Phase material properties and fluidization parameters are reported in Table 1. Monodisperse spherical beads of Pyrex ($d_p = 6\,mm$, $\rho_p = 2230\,kg/m^3$) have been fluidized in a concentrated aqueous solution (65% w/w) of potassium thiocyanate (KSCN) of density $\rho_f = 1400\,kg/m^3$ and viscosity $\mu_f = 3.8 \times 10^{-3}\,Pa.s$ at $T = 20°C$. At this temperature, refractive indices of both phases are matched, allowing the implementation of optical techniques such as high-speed video for the 3-D Lagrangian tracking of colored particles or high frequency Particle Image Velocimetry for the measurement of the velocity field in the liquid phase (Aguilar-Corona, 2008). Particle terminal velocity, V_t, is $0.24\,m/s$ and Reynolds number based on V_t is $Re_t = 530$. Inertia of the particles is characterized by a Stokes number here defined as $St_t = \frac{8\rho_p}{3\rho_f C_{Dt}} = 5.3$ (C_{Dt} is

the drag coefficient of a single particle at V_t, here equal to 0.8). Fluidization law and fluctuating motion of both phases have been measured by Aguilar-Corona (2008) in a range of fluidization velocities ranging between 0.17 and $0.05\,m/s$, corresponding respectively to be solid volume fraction ranging between 0.1 and 0.5. Details of the measurement techniques can be found in Aguilar-Corona (2008).

Liquid phase	ρ_f	$1400\,kg/m^3$
	μ_f	$3.8 \times 10^{-3}\,Pa.s$
Fluidization velocity	U_F	$0.17/0.15/0.12/0.09/0.073\,m/s$
Particles	ρ_p	$2230\,kg/m^3$
	d_p	$6 \times 10^{-3} m$
	V_t	$0.24\,m/s$
	Re_t	530
	St_t	5.3
Fluidization law	$U_{F0}(1-\phi_b)^n$	$n = 2.41$, $U_{F0} = 0.226\,m/s$

Table 1: Phase properties and fluidization parameters

3. Numerical model

Details of numerical approach and validation test cases are given in Vincent et al. (2014). The DNS approach is based on a one-fluid formalism of the incompressible Navier-Stokes equations with an algebraic adaptive augmented Lagrangian method used for pressure-velocity coupling (Implicit Tensorial Penalty Method, ITPM). The particles are considered as a fluid with specific rheological properties whose evolutions are modeled by the Navier-Stokes equations. This method enforces the solid behavior of the particles in the framework of Eulerian fixed grid. A Lagrangian Volume Of Fluid (VoF-Lag) method enables particle tracking while avoiding particle shape deformation and ensuring volume conservation of the solid phase. This approach provides a second order convergence in space and time.

In dense flows such as in fluidized beds, wall-particle and inter-particle collisions must be accounted for as well as lubrication. Fully resolved lubrication fluid layer between a particle and a wall requires a highly refined Eulerian grid at the scale of the particle (about 150 grid points per particle). However, such a refinement level is not affordable for the simulation of the present liquid-solid fluidized bed and a more appropriate sub-grid lubrication force model proposed by Brändle de Motta et al. (2013) has been used instead. Lubrication is activated at a dimensionless separation distance of $2\Delta x/d_p$ and the lubrication force is kept constant if the distance (scaled by the particle radius) is less or equal than 10^{-3}. When particles overlap, due to unresolved fluid equations at the subgrid scale, an inter-particle repulsive force is activated (a linear spring-dashpot (Hookean) model). The values of lubrication and collision models parameters have been optimized in Brändle de Motta et al. (2013). This model predicts a normal restitution coefficient (normalized by the reference value in vacuum, close to 1) that well matches the scaling law proposed by Legendre et al. (2006). Using the parameters of the studied fluidized bed and varying the normal collision velocity, the resulting normal coefficient of restitution is also in good agreement with the correlation of Legendre et al. (2006), as illustrated by Figure 1. The collision and lubrication force models for multiple particle-particle and particle-wall interactions are implemented in the Navier-Stokes equations as volume force terms, and their semi-implicit treatment avoids particle overlapping during the solving step of the flow field.

Figure 2 shows the computational domain. It has the same dimensions as the experimental fluidization column. It is composed of a parallelepipedic box of dimensions $0.08 \times 0.08 \times 0.64\,m$. The solid wall boundary of the cylindrical column is simulated using a Darcy penalty method (Khadra et al., 2000), consisting in adding a Darcy term in the momentum equations with a very small permeability ascribed to the cells located outside the cylindrical envelope. This method ensures a no-slip condition at the cylinder wall. A uniform distribution of fluid velocity is imposed at the bottom of the bed and a free outlet boundary condition is defined at the top of the bed. The domain is discretized with

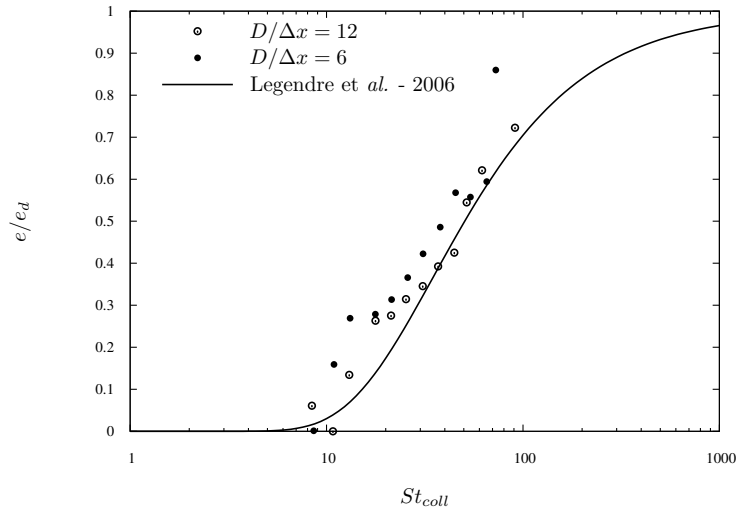

Figure 1: Normal restitution coefficient of collisions with respect to collisional Stokes number $St_{coll} = \frac{2}{9}\frac{Ru_{coll}\rho_p}{\mu_f}$: influence of the spatial resolution.

a uniform grid composed of 32 million cells ($160 \times 160 \times 1280$). Such a grid corresponds to a resolution of 12 cells per particle diameter. It is kept constant for all fluidization velocities.

At the beginning of the simulation, the particles were uniformly distributed in the domain with an equivalent solid concentration of 0.1 (the corresponding bed height is $0.47\,m$).

Both fluid and particles are at rest at the beginning of the first simulation, corresponding to a fluidization velocity $U_F = 0.17\,m/s$. After $10\,s$ of physical time simulation, particles reached a steady fluidization regime. In order to save computation time, for other test cases at lower fluidization velocities, the initial conditions were taken from the steady fluidized regime at $U_F = 0.17\,m/s$.

Simulations were carried out during a physical time of $20\,s$ with a time step of $\Delta t = 5 \times 10^{-4}\,s$ for each fluidization velocity studied and using 512 Intel Quad-Core in French supercomputing centers. The restitution time for each case is about 50 days in order to simulate $20\,s$ real time of bed flow. Figure 3 shows 3-D snapshots of particle distribution in the bed and illustrates the transient stage of the calculation after 5, 10 and 20 seconds ($U_F = 0.12\,m/s$). The bed settles

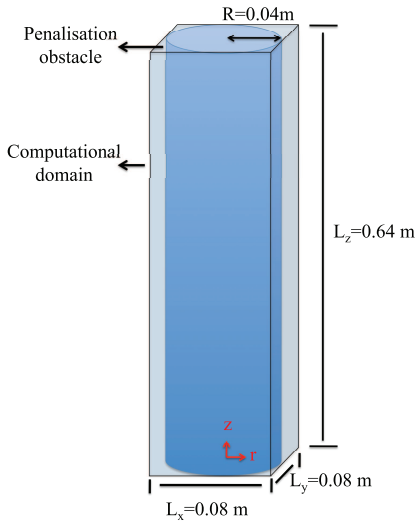

Figure 2: Geometry and dimensions of the computational domain.

down after 5 s and particle packing takes place within a steady volume. Another 5 seconds delay of simulation time is considered before performing statistics. Statistical averages presented in next section were therefore calculated over a 10 s period of simulation, 10 s after the beginning of each simulation (see figure 4).

4. Results and Discussions

Numerical results are compared to experimental data taken from Aguilar-Corona (2008). In experiments, averaged bed height was determined from video camera in slightly unmatched refractive index conditions. Measurement of this quantity at different fluidization velocities gives the fluidization law. Fluctuating motion of the particles was analyzed from the recording of 12 trajectories of marked particles during 3 minutes at a sampling frequency of 60 Hz. Fluctuating motion of the liquid phase was characterized from the acquisition of the velocity field in a median plane of the column, using high speed PIV (between 250 and 500 Hz) and a spatial resolution of $d_p/5$.

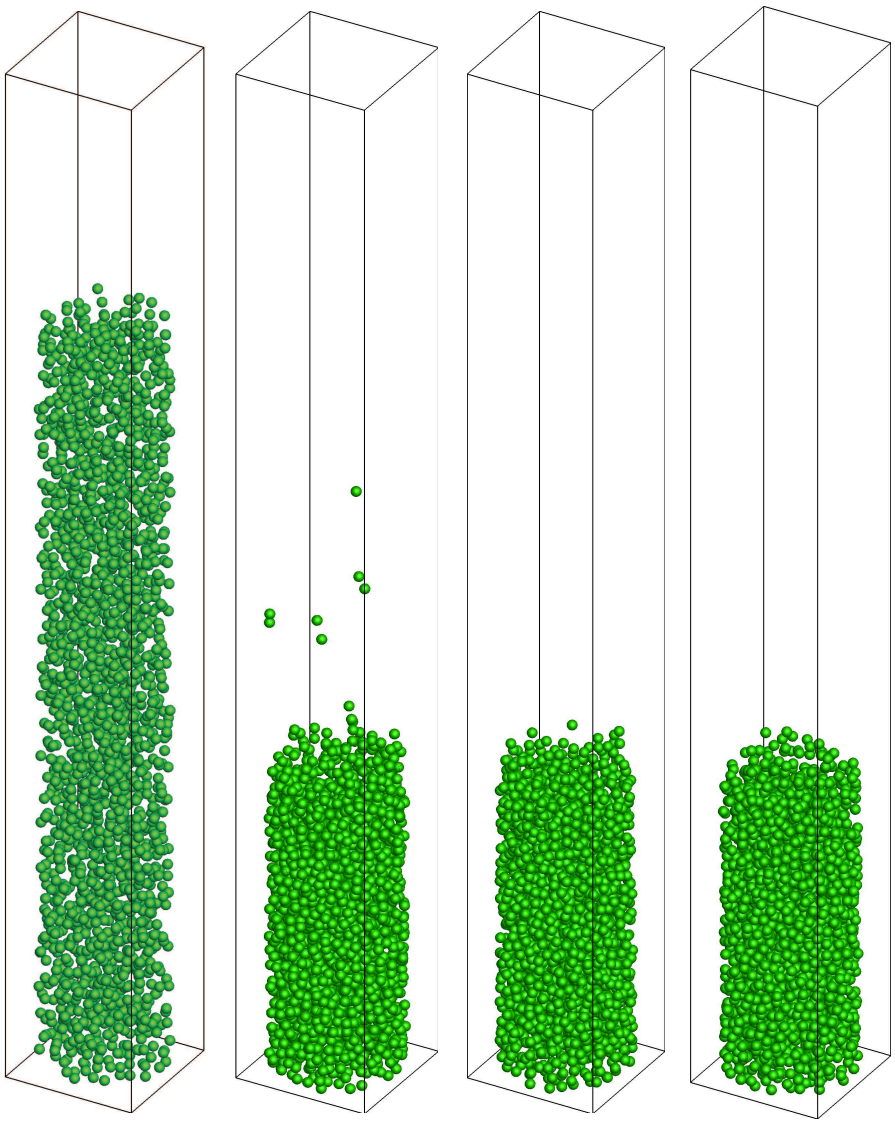

Figure 3: 3-D views of the simulated particles inside the bed (from left to right: $t = 0,\ 5,\ 10$ and $20\,s$).

4.1. Fluidization law

The fluidization law (relationship between the fluidization velocity and bed solid fraction) is the first step of validation of the numerical model, reflecting the macroscopic balance between buoyancy and drag forces. In order to calculate the bed solid concentration ϕ_b, the bed height h_b was computed using two different methods, which led to the same result.

First, the bed height was set equal to the time averaged maximum particle position in the axial direction. Figure 4 displays the time-evolution of this parameter at different fluidization velocities. After a transient period, it oscillates around a steady value for all cases investigated due to particle agitation. The intensity of fluctuations is a decreasing function of the fluidization velocity, with a maximum of the order of 5% for the lowest fluidization velocity.

Second, the bed height was also determined by averaging in time (during $10\,s$) and space (over the bed volume) a particle phase indicator function $\chi_p(\mathbf{x}, t)$. This function is defined on each Eulerian mesh cell, equal to 1 if the node is inside the particle and 0 if not. A vertical profile of the time-section average of the particle phase indicator function (or phase fraction) $\{\chi_p\}_{layer}$ as defined in equation (A.3), is shown by Figure 5 at different fluidization velocities. This quantity represents the solid volume fraction averaged in cylinders of diameter D and thickness Δz. So the integral of $\{\chi_p\}_{layer}$ layer along z is equal to $\phi_b h_b$.

Figure 5 shows that the phase fraction is rather homogeneous along the bed height but in the freeboard region a gradient of the solid volume fraction develops, becoming stiffer as the fluidization velocity is decreased. The bed height is then computed by applying a linear regression with a high order polynomial interpolation on the volume fraction profile at the interface between the bed and the freeboard region, and the z value of the inflection point of that function is defined as the bed height h_b.

Both estimations lead to close values of h_b for all velocities with a difference of a few percent. The bed solid fraction ϕ_b is then calculated according to:

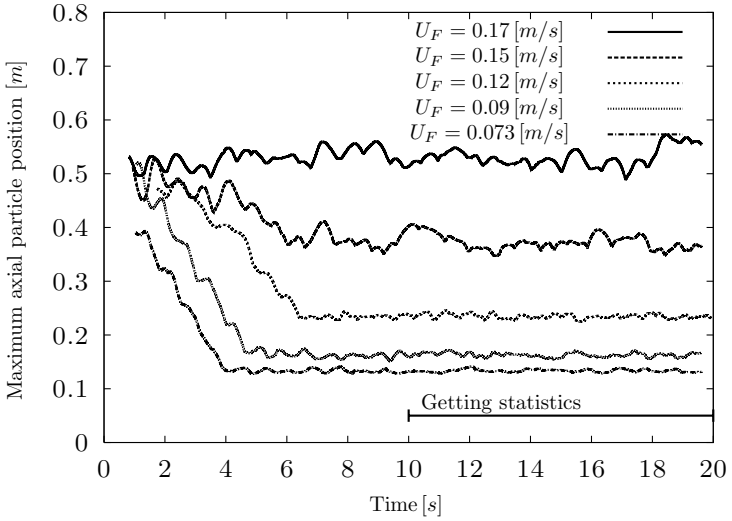

Figure 4: Time-evolution of maximum axial particle position at different fluidization velocities: $U_F = 0.17$, 0.15, 0.12, 0.09, $0.073\,m/s$ (resp. $\phi_b = 0.11$, 0.14, 0.22, 0.31, 0.39)

$$\phi_b = \frac{2}{3}\frac{n_p d_p^3}{h_b D^2} \tag{1}$$

Plotting the fluidization velocity as a function of the bed solid concentration ϕ_b gives the fluidization law. Figure 6 shows the bed solid concentration measured in DNS together with the experimental data of Aguilar-Corona (2008) and the correlation of Richardson and Zaki (1954):

$$U_F = U_{F0}(1 - \phi_b)^n \tag{2}$$

where n is a function of Re_t , U_F is the fluidization velocity and U_{F0} is the fluidization velocity leading to particles entrainment. The exponent value best fitting experimental data is $n = 2.41$ ($Re_t = 530$), and is in quite good agreement with the value predicted by Richardson-Zaki correlation at that particle Reynolds number ($n = 2.39$ for $Re_t > 500$). Experimental value of U_{F0} is found equal to $0.226\,m/s$, and the measured terminal velocity of the particles is $V_t = 0.24\,m/s$. The ratio of U_{F0}/V_t is equal to 0.94, which corresponds to the upper limit of the range of values of this parameter in liquid fluidization. Note

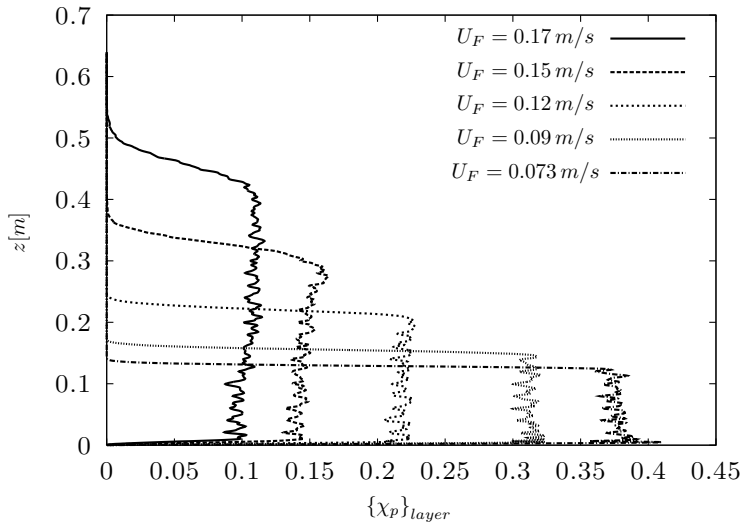

Figure 5: Axial profile of time-section average of particle phase fraction χ_p.

also that it is not related to the ratio d_p/D (Di Felice and Kehlenbeck (2000)). The agreement between experiments and numerical simulations is quite good, and to the best of our knowledge, this result is the first validation of particle resolved simulation of fluidization law in a full 3-D fluidized bed in that range of particle Reynolds number.

4.2. Particle trajectories and Lagrangian velocity signal

Figures 7 and 8 exhibit projections of 16 particle trajectories in the radial and vertical planes of the bed, for two different fluidization velocities (0.15 and $0.073\,m/s$). It can be observed that particle trajectories are quite sensitive to this parameter. At high fluidization velocity (low concentration), trajectories occupy all the bed space, with an apparent slight deficit of particles in the bed bottom zone (close to the flow inlet). For the same simulation time ($10\,s$), the space travelled by the same number of particle trajectories tends to reduce at higher concentration (lower fluidization velocity). This confinement effect can be clearly observed on the trajectory envelopes projected in the cross section ($x-y$ plane), with the development of dark spots near the bed wall, the signature of particle trapping over long-time periods. Additionally, the shape of the paths

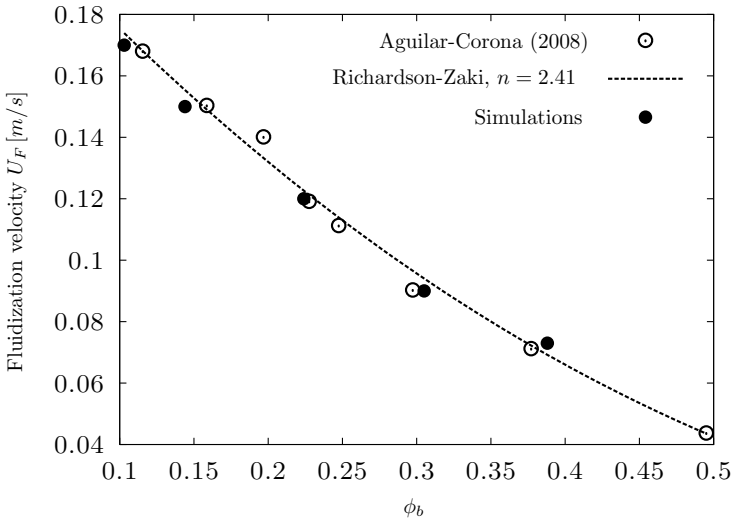

Figure 6: Fluidization velocity with respect to the bed solid concentration. ⊙: Aguilar-Corona (2008), − − −: (Richardson and Zaki, 1954)'s correlation with $n = 2.41$ and ●: present simulations.

becomes more and more angular as the bed is compacted, in response to the increase of inter-particle collisions. Overall, the multi-scale diffusive-like motion of the particles in the bed as calculated by the numerical simulations exhibits remarkable similarities with the experimental signals (12 particle trajectories recorded during more than 3 minutes), suggesting that the physics of the fluid-particle and particle-particle interactions are qualitatively well captured by the numerical model, in both dilute and dense regimes.

Figure 9 exhibits the instantaneous axial and radial particle velocity components following one particle trajectory for the case $\phi_b = 0.31$ ($U_F = 0.09\,m/s$). Numerical and experimental signals present qualitatively similar features, being composed of large scale, low frequency and small scale, higher frequency fluctuations. The amplitude of fluctuations is more pronounced on the axial component $U_{p,z}$ than on the transverse one, $U_{p,x}$. The frequency of the high amplitude velocity fluctuations is smaller on $U_{p,z}$ than on $U_{p,x}$ signals.

Modes of high frequency can be observed in the numerical signal, which is not the case of the experimental signal. Their occurrence could be inferred to

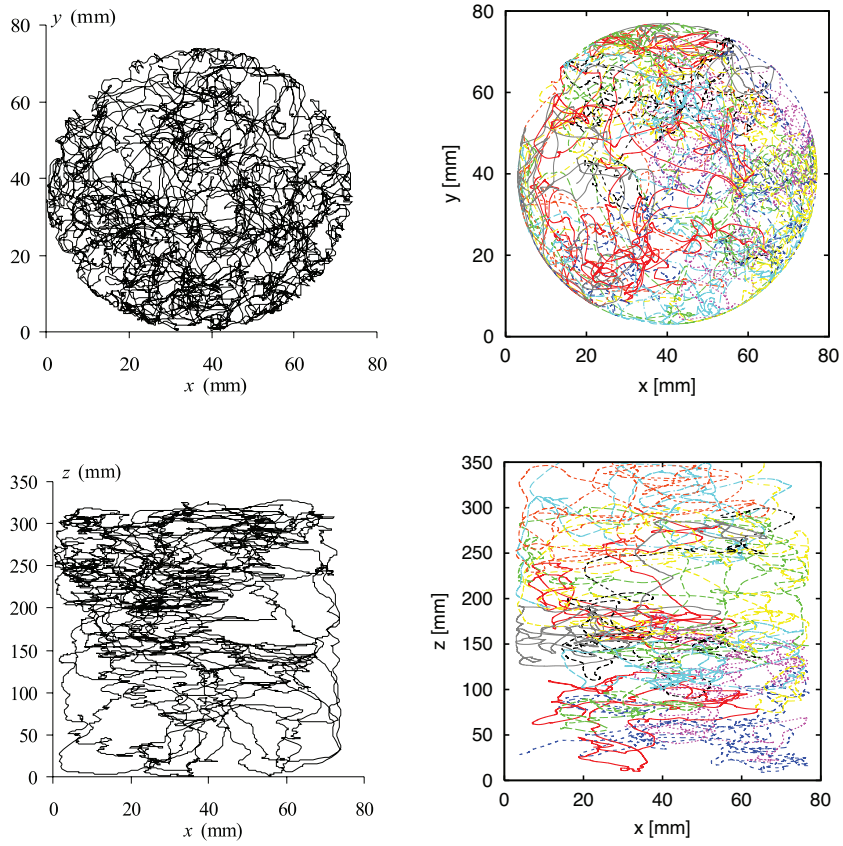

Figure 7: Projections of particle trajectories in $x-y$ plane (top) and $x-z$ plane (bottom). Left: Experimental data by Aguilar-Corona (2008) ($U_F = 0.15\,m/s, \phi_b = 0.14$), right: Simulations.

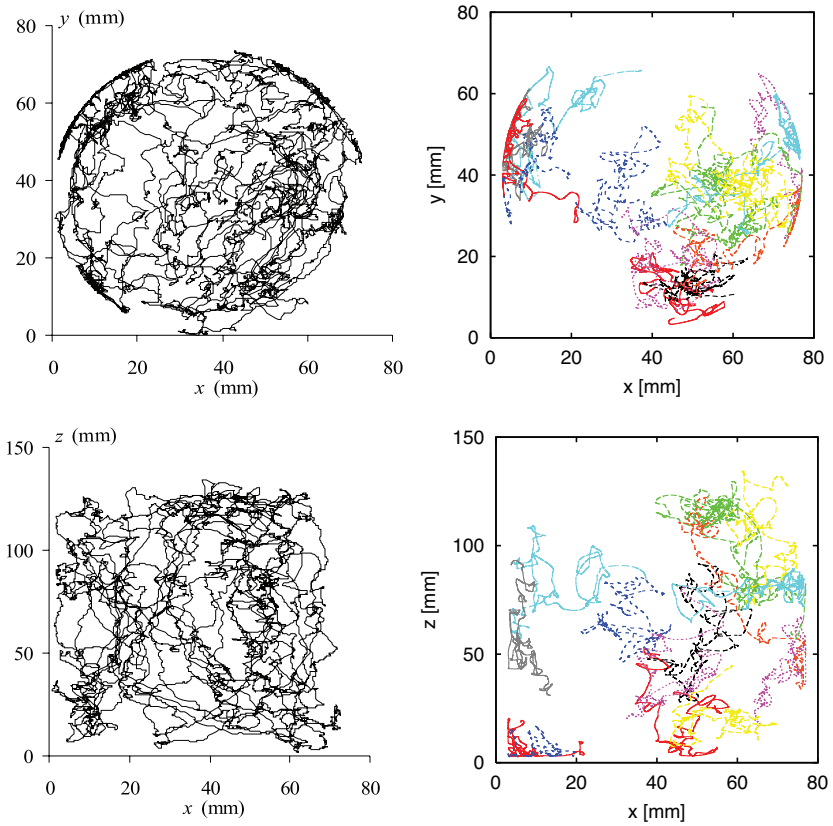

Figure 8: Projections of particle trajectories in $x-y$ plane (top) and $x-z$ plane (bottom). Left: Experimental data by Aguilar-Corona (2008) ($U_F = 0.073\,m/s, \phi_b = 0.38$), right: Simulations.

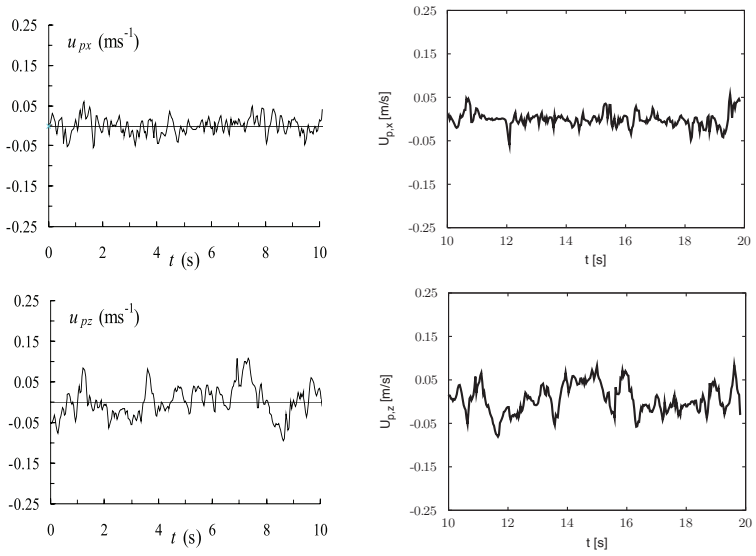

Figure 9: Experimental data by Aguilar-Corona (2008) (left) and simulation results of a particle Lagrangian velocity signal ($\phi_b = 0.31$; $U_F = 0.09\,m/s$). Top: Transverse and bottom: axial components.

the collisional model (used in the numerical simulations) that generates abrupt modification of the velocity upon collisions, whereas their absence in the experimental signal could be due to a filtering effect (velocity sampling frequency in the experiments: $30\,Hz$).

4.3. Recirculation

The low frequency, large amplitude fluctuations suggest the presence of large-scale coherent structures. Figure 10 shows time and azimuthal average of the particle velocity field defined as $\langle u_p \rangle_{ann\Delta z}$. It represents the average of particle velocity in a hollow cylinder of inner radius r and outer radius $r + \Delta r$ and of thickness Δz (c.f. Appendix). Fields of $\langle u_p \rangle_{ann}$ reveal the presence of a localized large-scale recirculation in the lower section of the bed, size of which compares with the bed diameter. For both concentrations $\phi_b = 0.31$ ($U_F = 0.09\,m/s$) and $\phi_b = 0.39$ ($U_F = 0.073\,m/s$), particles preferentially rise up near the bed axis and flow downward near the wall. The upward velocity is larger than the

downward velocity owing to mass conservation. The shape of particle path-lines indicates that the recirculation is stronger in the bottom of the bed, confirming the existence of a large-scale toroidal motion above the flow inlet detected in the trajectography experiments (cf Figure 7). Figure 11 displays radial profiles of the axial component of particle velocity averaged in time and over the bed height $\langle u_{p,z} \rangle_{ann}$ ($\langle . \rangle_{ann}$ denotes the average of $\langle . \rangle_{ann\Delta z}$ over bed height). When radial position tends towards zero, the density of particles in the control hollow cylinder is weak, and statistics of particle velocity are not fully converged near the bed axis in the 10 seconds integration window. This lack of convergence near the bed axis is more pronounced at highest fluidization velocities (lowest bed solid fraction). As a general trend particle motion in the bed is upward in the middle of the bed and downward in the near wall region (between 0.2 and 0.6 column radius from the wall). When particles are very close to the wall they tend to rise along the wall. Note that the magnitude of this mean motion is an order of magnitude smaller than the particle r.m.s. velocity presented in the next section.

4.4. Particle and fluid velocity variance

The average of the velocity variance of particles in the whole bed is computed as follows:

$$< u_{p,i}^{'2} >=< (u_{p,i} - < u_{p,i} >_{ins})^2 > \quad (3)$$

$< . >$ denotes the time-space average defined in the Appendix, $u_{p,i}$ is the i component of the instantaneous Lagrangian particle velocity, and the symbol $< . >_{ins}$ refers to the average operator as $< . >$ at each time step.

The variance of radial particle velocity as a function of vertical position in the bed, calculated in horizontal layers of thickness Δz and diameter D, is noted $\left\langle u_{p,x}^{'2} + u_{p,y}^{'2} \right\rangle_{layer}$ (see Appendix). The axial profile of this quantity normalized by the radial velocity variance in the whole bed is reported in Figure 12 (top) at different fluidization velocities. Profiles collapse on a single curve, and exhibit a rather homogeneous distribution of radial velocity variance in a large portion of the bed, slightly increasing from 0.9 to 1.1 between $z/h_b = 0.2$

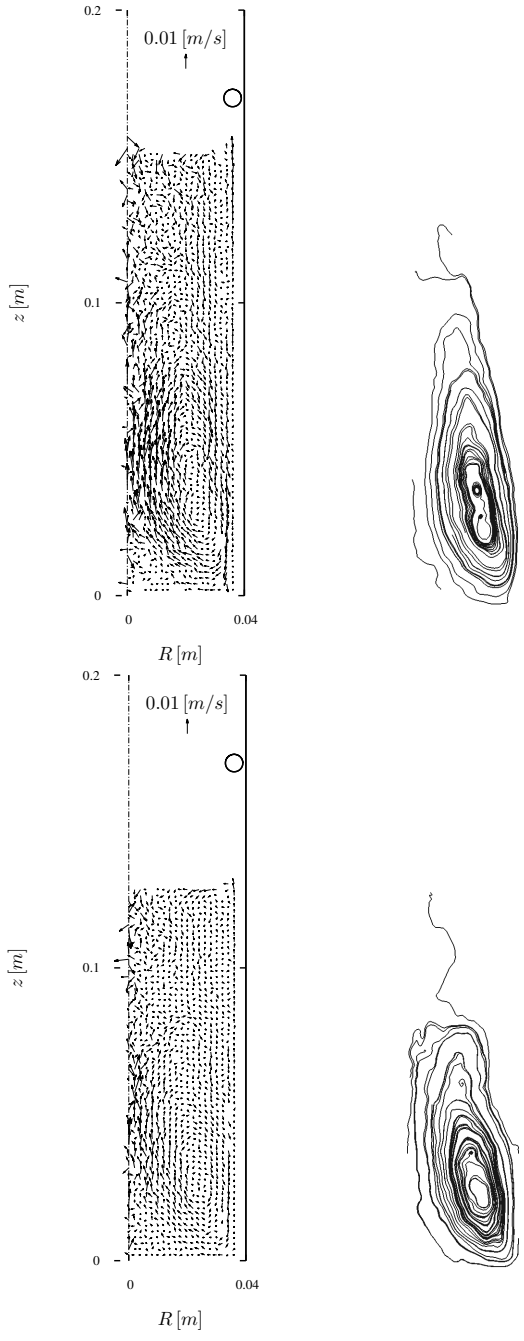

Figure 10: Averaged particle velocity field and streamlines for the case $U_F = 0.09\, m/s$ (top) and $U_F = 0.073\, m/s$ (bottom).

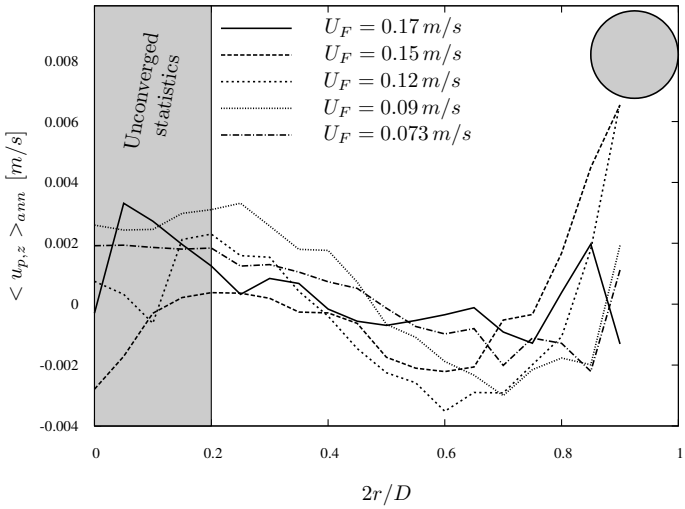

Figure 11: Radial profile of axial velocity averaged over the bed height.

and $z/h_b = 0.9$. In the bottom part of the bed, $0 < z/h_b < 0.2$, the variance is smaller and is growing from 0.5 to 0.9. In the top part of the bed ($z/h_b > 0.9$), the occurrence of peaks of large amplitude in the near-freeboard region results from the transition of fluid velocity between a concentrated medium and a free-particle domain, getting sharper as the bed solid fraction increases (or as the fluidization velocity decreases).

The variance of axial particle velocity component as a function of radial position in the bed is calculated in vertical hollow cylinder of thickness Δr and is noted $\left\langle u'^2_{p,z} \right\rangle_{ann}$ (see Appendix). The radial profiles of normalized variance $\frac{\left\langle u'^2_{p,z} \right\rangle_{ann}}{\left\langle u'^2_{p,z} \right\rangle}$ are shown in figure 12 (bottom) for various fluidization velocities. The axial velocity variance is minimum in the core of the bed and maximum near the wall, due to the transition between negative velocities in the recirculation loop to positive values very near the wall (see Figure 11). However, the shape of the profiles depends on the fluidization velocity. At highest fluidization velocity (minimum bed solid fraction), the profile shows a marked gradient along bed radius (from 0.55 to 1.25), which tends to flatten as the fluidization velocity decreases. At largest bed concentration (smallest fluidization velocity) the shape

of the profile is rather homogeneous varying from 0.9 in the core of the bed to 1.1 near the wall.

Figure 13 shows the variance of particle velocity components in the whole bed (eq. (3)) as a function of bed solid volume fraction and compared to experimental data. The numerical data are reasonably in good agreement with experiments, showing a strong decrease of the agitation with the concentration. However at the largest fluidization velocity (lowest concentration), the simulation overpredicts the experimental value by a factor of two. At larger concentrations the trend is reversed, numerical results underpredict experimental values. The same behavior is observed for both components (axial and transverse).

The particle agitation in the fluidized bed is not isotropic: the variance of the axial component of velocity is stronger than that of the transverse component (isotropy of the fluctuations in the transverse plane was checked). This behavior is already well known in gravity driven gas-solid suspensions, like in sedimentation. The anisotropy coefficient k_{anis} is defined as the ratio of the particle velocity variance in flow direction (z) to that in the transverse plane (x, y):

$$k_{\text{anis}} = \sqrt{\frac{< u'^2_{p,z} >}{\frac{1}{2}(< u'^2_{p,x} > + < u'^2_{p,y} >)}}. \tag{4}$$

Its evolution as a function of bed solid fraction is shown in Figure 14. Numerical predictions (1.5 in average) are close to the experimental values (1.6) and nearly constant in the range of bed solid fraction investigated, unlike sedimentation case at low Reynolds number where anisotropy is decreasing as particle concentration increases (Nicolai et al. (1995)). This result emphasizes the leading role of large-scale motion in the agitation of particles fluidized by a liquid at high Re_p. Note that despite the differences observed between numerical and experimental data at lowest and highest solid fraction, the correct prediction of anisotropy coefficient over all the concentration range investigated suggests that the structure of the large scale motion is well captured by the numerical model.

The total fluid energy, E_f and particle fluctuating kinetic energy,E_p with

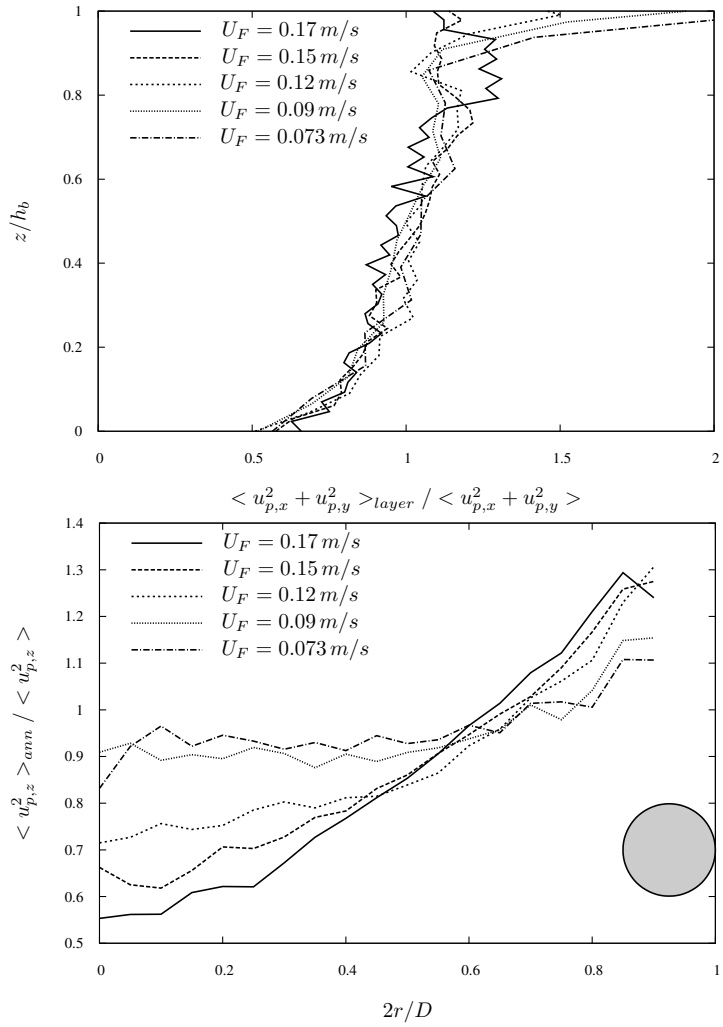

Figure 12: Top: Axial profile of transverse particle agitation; Bottom: Radial profile of axial particle agitation.

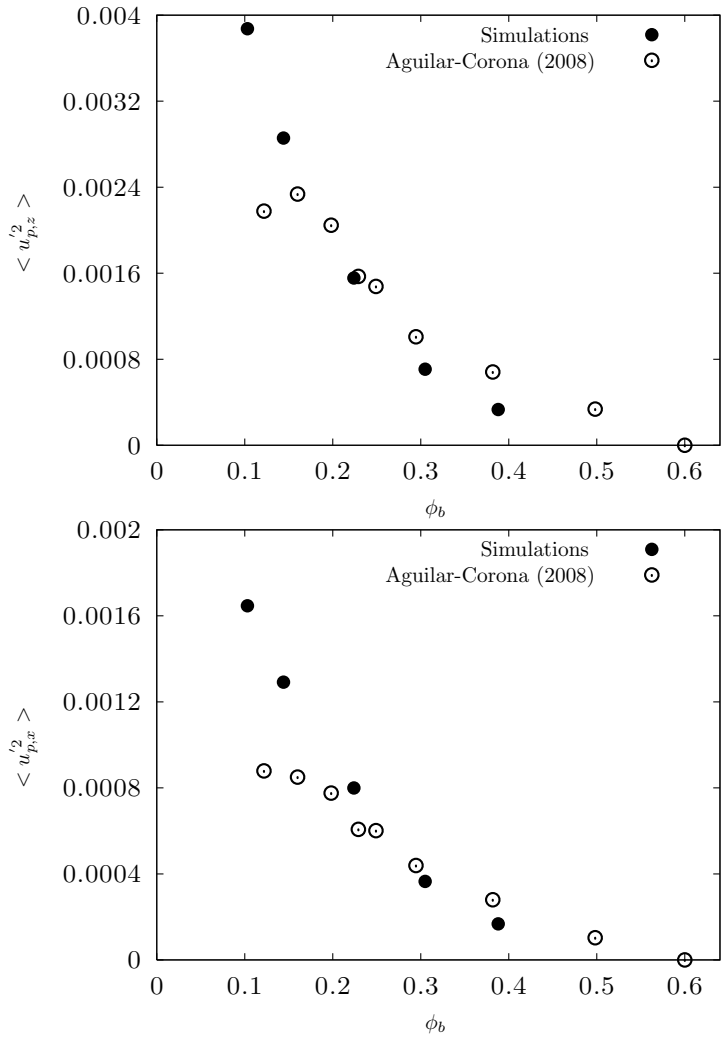

Figure 13: Variance of particle velocity with respect to the bed solid concentration. Top: axial component, Bottom: transverse component. ⊙:Aguilar-Corona (2008) and ●: present simulations.

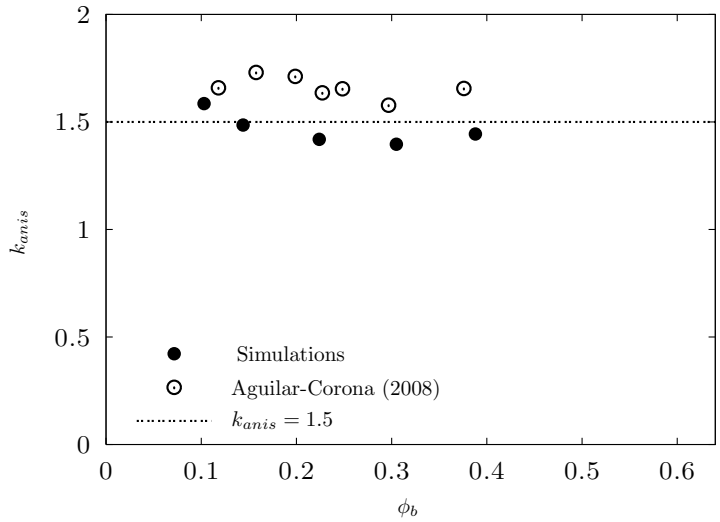

Figure 14: Anisotropy coefficient of the particle velocity fluctuations with respect to the bed solid concentration. ⊙:Aguilar-Corona (2008) and ●: present simulations.

respect to the bed solid volume fraction are shown in Figure 15. For the particle phase it is computed as:

$$E_p = \frac{1}{2}\left(2\left\langle u_{p,x}^{'2}\right\rangle + \left\langle u_{p,z}^{'2}\right\rangle\right) \tag{5}$$

and for the fluid phase:

$$E_f = \frac{1}{2}(2\left[u_{f,x}^{'2}\right]_{plane} + \left[u_{f,z}^{'2}\right]_{plane}) \tag{6}$$

where $[.]_{plane}$ denotes the Eulerian average in a vertical median plane (see definition in Appendix). The choice of this average is driven by the correspondence with experimental data obtained with High Frequency PIV in a vertical median plane of the bed (Aguilar-Corona (2008)).

Figure 15 shows that the fluid fluctuating kinetic energy with respect to the solid volume fraction does also fit well experimental data obtained from HF PIV measurements, except at low phase fraction where it underestimates experimental data. Interestingly, the fluctuation level of the liquid phase is always significantly larger than that of the solid phase in all the range of solid phase fraction investigated. The ratio E_f/E_p is a growing function of ϕ_b.

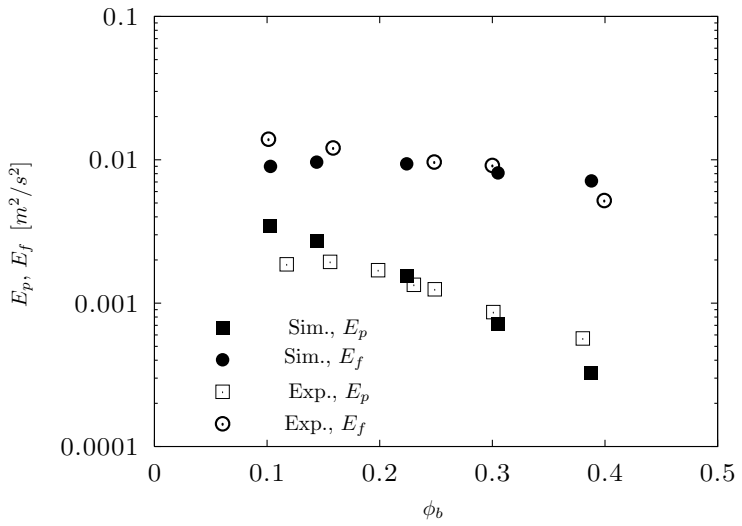

Figure 15: Fluctuating kinetic energy of fluid phase E_f and particle phase E_p. Solid symbols: simulations, empty symbols: Aguilar-Corona (2008).

The particle and fluid agitation are shown here at moderate concentration range, while one can expect two limiting behaviors at small and high volume fractions.

In the very dilute regime ($\phi_b \to 0$), particle agitation is expected to be close to that observed in a dilute turbulent pipe flow. This regime corresponds to a fluidization velocity equal to the particle terminal velocity (particle entrainment). In the present case, particle terminal velocity is $V_t = 0.24\, m/s$, and flow Reynolds number is $Re_f = \frac{\rho_f V_t D}{\mu_f} \sim 7 \times 10^3$, with a wall friction velocity derived from Blasius law equal to $0.016\, m/s$. The corresponding fluctuating kinetic energy is about $3 \times 10^{-4}\, m^2/s^2$, which is nearly two orders of magnitude smaller than E_f measured (in the experiments and simulations) at $\phi_b = 0.1$. Neglecting the fluid turbulent modulation by the particles in the very dilute limit, an estimation of particle fluctuating kinetic energy can be scaled as that of the continuous phase weighted by a function of particle Stokes number (Tchen (1947), Deutsch and Simonin (1991)), here defined as the ratio of particle response time to the fluid turbulent time macro-scale. For the present system, such an estimate gives in very dilute regime the same order of magnitude for $E_p|_{\phi_b \to 0}$ as

$E_f|_{\phi_b \to 0}$ (taken equal to that of a steady turbulent pipe flow), and therefore is one order of magnitude smaller than the particle fluctuating kinetic energy measured at the lowest volume fraction $E_p|_{\phi_b=0.1}$. Therefore, both particle and fluid agitation should increase at very low concentration, without however being captured by the present measurements. From these estimations, we conclude that the fluctuating energy for both phases at $\phi_b = 0.1$ is far larger than the very dilute limit, which means that the fluctuations are dominated by strong particle-fluid flow coupling. Consequently, if we decompose the fluid fluctuating energy in two components, one of them induced by large scale collective motion and the other one due to small scale fluid-particle wake turbulence (also referred to in the literature as pseudo-turbulent kinetic energy), $E_f = \widetilde{E_f} + \delta E_f$, the second component would be far greater than the first one. Note that a rigorous formulation of the energy decomposition is reviewed in Fox (2014). The strong coupling seems to be intrinsic to liquid fluidization whereas the opposite is true in gas fluidization, which is essentially related to difference in particle inertia.

When the concentration increases, the particle fluctuating energy decreases. At large volume fraction ($\phi_b \to \phi_{max}$), the particle phase approaches a porous media. E_p vanishes whereas E_f remains finite, meaning that velocity fluctuations of both phases become uncorrelated. In this limit, large scale motion disappears and flow fluctuations derive from the so-called pseudo-turbulence ($E_f = \delta E_f$, or equivalently $\widetilde{E_f} \approx 0$). Interestingly, the decrease of fluid fluctuating energy with concentration $E_f|_{\phi_b=0.1} - E_f|_{\phi_b \to \phi_{max}}$ is close to $E_p|_{\phi_b=0.1}$, suggesting that the particle fluctuating energy at low concentration is mainly driven by the flow large scale fluctuating motion $\widetilde{E_f}$.

Note that in figure 15, the decay with bed solid fraction of particle agitation is stiffer in numerical than in experimental curves, whereas the reverse trend is observed with fluid agitation. The origin of the differences observed between numerical and experimental data is difficult to identify. First, statistics on the particle phase are not derived in the same way (2133 particles during 10 seconds for the numerical data, 12 trajectories during 3 minutes for the experimental data). Second, in this range of particle Reynolds number ($Re_t = 530$), the flow

is probably under-resolved with 12 cells per particle diameter and the small-scale structures of the flow are probably partially filtered (Uhlmann and Dušek (2014)). The resulting particle relative velocity prior to collisions, and therefore the numerical treatment of collisions can be affected. All these issues require to be addressed separately in order to quantify their contribution to the calculation of both phases agitation.

4.5. Particle fluctuation time scales

The time-scale (macro-scale) characteristic of particle agitation can be derived from the computation of autocorrelation function of axial and radial velocity components (given in Appendix). The autocorrelation function is shown in Figure 16 for two bed solid volume fractions (0.12 and 0.3, respectively corresponding to 0.17 and $0.09\,m/s$). After the initial step of continuous decay, both components exhibit a large oscillating behavior at long times. Origin of these oscillations is likely due to the contribution of the localized recirculation zones in the bed bottom section (see Figure 10), which seems to be supported by the observation that period of oscillations decreases as the fluidization velocity is decreasing, i.e. when the bed height is decreasing. Comparison of numerical and experimental curve shapes exhibits some discrepancies. At short times ($< 0.4\,s$) curves behave the same with a stronger decay of the transverse component compared to the axial velocity component. At longer times, experimental curves decay much more slowly than calculated curves, which oscillate around the abscissa axis. This is particularly noticeable for the autocorrelation function of the particle axial velocity component. Regarding the radial motion, the decorrelation time of velocity fluctuations, that is to say the time at which the curves reach the horizontal axis is nearly constant for both bed solid fractions and compares well with experimental data, close to $0.3\,s$. The decorrelation time of axial fluctuations as predicted by the numerical data is significantly smaller compared to the experimental data and its evolution with the bed solid fraction is reversed. When the bed solid volume fraction increases from 0.12 to 0.3, it decreases from 0.5 s to 0.3 s whereas experimental data shows an increase from

1.8 s to 2.1 s. It is believed that the absence of the oscillatory behavior on the experimental curves is mainly due to a subsampling of the recirculation zones by the tracked marked particles, which statistical weight in the numerical signal must be strengthened by the localized and steady nature of such structures. As these structures are anti-diffusive, they hinder the long time diffusive behavior observed in the experimental trajectories. This result emphasizes the limits of the comparison between ensemble average short-time autocorrelation function over all the particles (which corresponds to the numerical data processing) and the calculation of same quantity over long-time trajectories (experimental data processing).

Interparticle collision frequency has been also computed using the collision detection model, which is activated if particles overlap during the lubrication step (see section 3). The frequency of collisions is then defined as the inverse of the averaged time between two consecutive collisions for each particle and averaged over all the particles in the bed and over time. Consequently, only the average detection of elastic collisions can be achieved based on such a method, i.e. when the restitution coefficient is non-zero. As shown by Figure 1, such a condition is valid when the collision Stokes number ($St_{coll} = \frac{1}{9}\frac{\rho_p d_p u_{coll}}{\mu_f}$) is roughly larger than 10. The average collision frequency f_{coll} is shown in Figure 17 as a function of global bed solid volume fraction ϕ_b and compared to the experimental data of Aguilar-Corona et al. (2011) based on a threshold value of particle acceleration. A fairly good agreement between numerical and experimental data is observed in a range of bed solid volume fraction up to 25%. At 30%, the agreement is less good and for higher bed solid volume fraction, the collision frequency is decreasing and tends towards zero when ϕ_b approaches the maximum packing. The same trend is observed with both experimental and numerical data, illustrating the transition between damped elastic to fully damped collisions (normal restitution coefficient equal to zero). Collisional Stokes number is continuously decreasing as the solid volume fraction increases due to the decrease of particle agitation. Above $\phi_b = 0.3 - 0.4$, the collision Stokes number based on the transverse fluctuating velocity becomes smaller than 10 and the

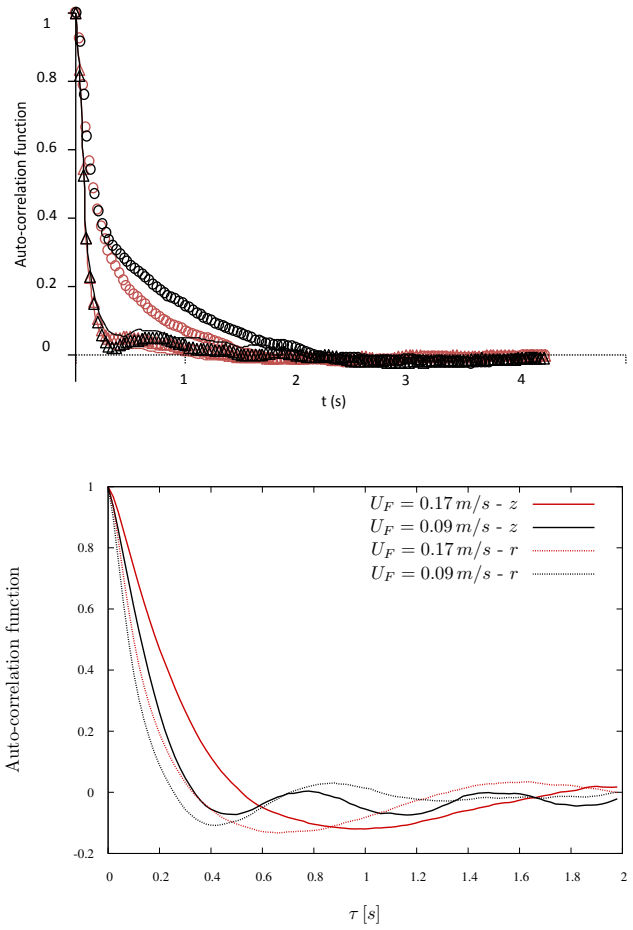

Figure 16: Particle velocity autocorrelation functions measured in Top: experiments (Circles: axial component. Triangles: radial component. Black : $\phi_b = 0.3$. Red=$\phi_b = 0.12$) and Bottom: Numerical simulation results.

.

restitution coefficient becomes smaller than 0.05 (see Figure 1), which makes the collisions difficult to detect from either numerical or experimental signals.

Below 0.3, the dimensionless collision frequency is well predicted by the numerical model. It remarkably fits the theoretical expression derived from the kinetic theory (noted KTFG in Figure 17). From the scaling of the collision time, $d_p/\sqrt{\frac{3}{4}\left(\langle u'^2_{p,x} + u'^2_{p,y}\rangle\right)}$ that can be identified to $d_p/\sqrt{\frac{3}{2}\theta_p}$ in KTGF, one can conclude that the transverse fluctuating motion of particles is the correct characteristic velocity scale to be considered for the collisions in the fluidized bed. This is consistent with Février et al. (2005) and Fox (2014) who suggested that the total particle velocity fluctuations can be decomposed in large and small scale fluctuations $E_p = \widetilde{E_p} + \delta E_p$. The first part contains particle large scale motion represented by the streamlines of Figure 10. It is approximately equal to the particle velocity variance in the axial direction and is fully coupled to the flow large scale motion via the buoyancy force and the non-uniform two-phase mixture density field ($\widetilde{E_p} \approx \widetilde{E_f}$). The second part accounts for random uncorrelated motion (transverse fluctuations), similar to Brownian motion resulting from collisions, usually referred to as granular temperature $\frac{3}{2}\theta_p$ in gas-solid flows. Note that the measured and calculated particle velocity variances (figure 13) suggest that $\widetilde{E_p}/\delta E_p > 1$ in liquid fluidization but this ratio is expected to decrease with particle inertia (Février et al., 2005).

5. Conclusions

Particle resolved simulations of a liquid-solid fluidized bed were performed using a one-fluid formulation of the incompressible Navier-Stokes equations, where the pressure-velocity coupling is provided by an algebraic augmented Lagrangian method and particles presence is modeled with an implicit penalty fictitious domain method, sub-grid scale lubrication force and soft-sphere collision models. We carried out simulations in a fully 3-D fluidized bed experimentally investigated by Aguilar-Corona (2008) on a structured uniform Eulerian grid at

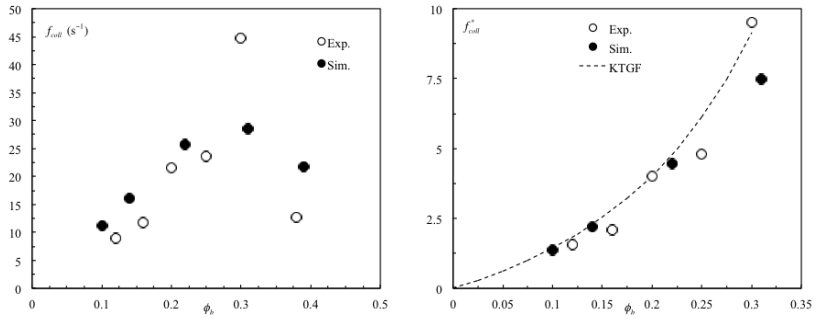

Figure 17: Collision frequency with respect to the bed solid volume fraction (left), non-dimensional collision frequency (right) $f^*_{coll} = f_{coll} \frac{d_p}{\sqrt{\frac{3}{4}\left(\left\langle u'^2_{p,x} + u'^2_{p,y} \right\rangle\right)}}$ compared to theoretical expression derived from KTGF $f^*_{coll} = 24\sqrt{\frac{2}{3\pi}}\phi_b g_0$ with $g_0 = \left(1 - \frac{\phi_b}{\phi_m}\right)^{-2.5\phi_m}$ and $\phi_m = 0.585$.

various fluidization velocities. Simulation results show the ability of the numerical approach to reach a steady regime of fluidization, and perfectly reproduce the experimental fluidization law. The instantaneous flow field exhibits small and large-scale motion in both phases. This behavior is observed in all range of fluidization velocity investigated, from dilute ($\phi_b = 0.11$) to dense regimes ($\phi_b = 0.39$). As the bed solid concentration is increased, the agitation of both phases is decreased, and the experimental trend is well reproduced except in the case of the lowest global concentration (highest fluidization velocity). However, the anisotropy of the agitation of particles is well predicted and is shown to be independent of the bed global concentration, reproducing the experimental trend. Fluid velocity variance in the bed is larger than that of the particle phase up to an order of magnitude at high concentration, in agreement with the experimental data. The results obtained at different fluidization velocities (or particle Reynolds numbers) suggest the following image. The fluid velocity fluctuations in the liquid fluidized bed result mainly from pseudo-turbulence generated by particle wakes, the particle velocity fluctuations in the axial direction follow the large scale flow motion whereas they are mainly driven by collisions in the transverse plane.

Overall, comparison between numerical and experimental instantaneous fields and averaged quantities tend to demonstrate that the physics of particle-fluid and interparticle interactions are well captured by the present numerical approach. The numerical database generated by this work will serve as a basis for a future support of statistical models for liquid fluidization. One can take advantage of the numerical data to provide quantities that can hardly be obtained in experiments, like pair distribution function, two-point correlations and intercorrelation of fluctuating quantities (particle velocity concentration, pressure gradient-concentration, fluid-particle velocities).

Acknowledgements

This work was granted access to the HPC resources of CINES under the allocation x20142b6115 made by GENCI (Grand Equipement National de Calcul Intensif) and of CALMIP under the allocation p0633 (Calcul en Midi-Pyréenés). This work has been supported by the research federation FERMaT (FR CNRS 3089).

Appendix A. Definition of the statistical operators.

The average operators of a quantity ϕ are defined in a Eulerian or Lagrangian way, whether ϕ describes the behavior of the continuous or discrete phase. The different average operators are explicitly defined in this section.

–Lagrangian averages–

- Arithmetic average on the ensemble of particles

$$\langle \phi \rangle = \frac{1}{\Delta T} \int \frac{1}{N_p} \sum_{n=1}^{N_p} \phi_n(t) dt \tag{A.1}$$

  where ϕ_n is a variable associated to the n^{th} particle. N_p is the total number of particles, and ΔT is the total simulation time. The time step

for statistical calculations of the Eulerian phase is 50 times the simulation time step.

- Average over cylindrical shells of height h_b and thickness Δr such that $\mathcal{H}(\mathbf{x}, r, \Delta r) = \{1 \text{ if } r < \|\mathbf{x} - \mathbf{x} \cdot \mathbf{e}_z\| < r + \Delta r \text{ else } 0\}$.

$$\langle \phi \rangle_{ann} = \frac{\int \sum_{n=1}^{N_p} \phi_n(t) \mathcal{H}(\mathbf{x}_n(t), r, \Delta r) dt}{\int \sum_{n=1}^{N_p} \mathcal{H}(\mathbf{x}_n(t), r, \Delta r) dt} \tag{A.2}$$

- Average over a disk of diameter D and thicknes Δz, such that $\mathcal{H}(\mathbf{x}, z, \Delta z) = \{1 \text{ if } z < \|\mathbf{x} \cdot \mathbf{e}_z\| < z + \Delta z \text{ else } 0\}$.

$$\langle \phi \rangle_{layer} = \frac{\int \sum_{n=1}^{N_p} \phi_n(t) \mathcal{H}(\mathbf{x}_n(t), z, \Delta z) dt}{\int \sum_{n=1}^{N_p} \mathcal{H}(\mathbf{x}_n(t), z, \Delta z) dt} \tag{A.3}$$

–Eulerian averages–

- Average over the Eulerian grid with N_{cells} the number of cells defined only in the part of the fluidized bed laden with particles.

$$\{\phi\} = \frac{1}{\Delta T} \int \frac{\sum_{i=1}^{N_{cells}} \phi_i}{N_{cells}} dt \tag{A.4}$$

where ϕ_i is the value of the variable ϕ of the continuous phase defined on the i^{th} cell.

- Average over a disck of diameter D and thicknes Δz,

$$\{\phi\}_{layer} = \frac{\int \sum_{i=1}^{N_{cells}} \phi_i \mathcal{H}(\mathbf{x}_i, z, \Delta z) dt}{\int \sum_{i=1}^{N_{cells}} \mathcal{H}(\mathbf{x}_i, z, \Delta z) dt} \tag{A.5}$$

where $\mathbf{x}_i$ is the position of the i^{th} cell.

- Phase average over the Eulerian grid

$$[\phi] = \frac{\int \sum_{i=1}^{N_{cells}} \phi_i (1 - \chi_i) dt}{\int \sum_{i=1}^{N_{cells}} (1 - \chi_i) dt} \tag{A.6}$$

where χ_i is the solid volume fraction of the i^{th} cell.

- Phase average on a plan $\mathcal{P} = \{\mathbf{x}, \mathbf{x} \cdot \mathbf{e}_y = 0\}$.

$$[\phi]_{plan} = \frac{\int \sum_{i=1}^{N_{cells}} \phi_i (1 - \chi_i) \delta_{i \in \mathcal{P}} dt}{\int \sum_{i=1}^{N_{cells}} (1 - \chi_i) \delta_{i \in \mathcal{P}} dt} \tag{A.7}$$

References

Aguilar-Corona, A., 2008. Agitation of particles in a liquid fluidize bed: Experimental study. Ph.D. thesis. University of Toulouse.

Aguilar-Corona, A., Zenit, R., Masbernat, O., 2011. Collisions in a liquid fluidized bed. International Journal of Multiphase Flow 37, 695–705.

Chouippe, A., Uhlmann, M., 2015. Forcing homogeneous turbulence in direct numerical simulation of particulate flow with interface resolution and gravity. Physics of Fluids 27, 123301.

Corre, C., Estivalezes, J.L., Vincent, S., Simonin, O., 2010. Direct numerical simulation of a liquid-solid fluidized bed computational techniques for multiphase flows, in: 7th International Conference on Multiphase Flow - ICMF 2010 Proceedings.

Derksen, J., 2014. Simulations of scalar dispersion in fluidized solid–liquid suspensions. AIChE Journal 60, 1880–1890.

Derksen, J.J., Sundaresan, S., 2007. Direct numerical simulations of dense suspensions: wave instabilities in liquid-fluidized beds. Journal of Fluid Mechanics 587, 303–336.

Deutsch, E., Simonin, O., 1991. Large eddy simulation applied to the motion of particles in stationary homogeneous fluid turbulence, in: Turbulence Modification in Multiphase Flows, ASME FED, pp. 35–42.

Di Felice, R., Kehlenbeck, R., 2000. Sedimentation velocity of solids in finite size vessels. Chemical engineering & technology 23, 1123–1126.

Duru, P., Guazzelli, É., 2002. Experimental investigation on the secondary instability of liquid-fluidized beds and the formation of bubbles. Journal of Fluid Mechanics 470, 359–382.

Février, P., Simonin, O., Squires, K., 2005. Partitioning of particle velocities in gassolid turbulent flows into a continuous field and a spatially uncorrelated

random distribution: theoretical formalism and numerical study. Journal of Fluid Mechanics 533, 1–46.

Fox, R., 2014. On multiphase turbulence models for collisional fluidparticle flows. Journal of Fluid Mechanics 742, 368424.

Gevrin, F., Masbernat, O., Simonin, O., 2008. Granular pressure and particle velocity fluctuations prediction in liquid fluidized beds. Chemical Engineering Science 63, 2450–2464.

Khadra, K., Angot, P., Parneix, S., Caltagirone, J.P., 2000. Fictitious domain approach for numerical modelling of Navier–Stokes equations. International Journal for Numerical Methods in Fluids 34, 651–684.

Legendre, D., Zenit, R., Daniel, C., Guiraud, P., 2006. A note on the modelling of the bouncing of spherical drops or solid spheres on a wall in viscous fluid. Chemical Engineering Science 61, 3543–3549.

Brändle de Motta, J.C., Breugem, W.P., Gazanion, B., Estivalezes, J.L., Vincent, S., Climent, E., 2013. Numerical modelling of finite-size particle collisions in a viscous fluid. Physics of Fluids 25, 083302.

Nicolai, H., Herzhaft, B., Hinch, E., Oger, L., Guazzelli, E., 1995. Particle velocity fluctuations and hydrodynamic self-diffusion of sedimenting non-brownian spheres. Physic of Fluids 6, 3936–3944.

Pan, T.W., Joseph, D.D., Bai, R., Glowinski, R., Sarin, V., 2002. Fluidization of 1204 spheres: simulation and experiment. Journal of Fluid Mechanics 451, 169–191.

Richardson, J., Zaki, W., 1954. The sedimentation of a suspension of uniform spheres under conditions of viscous flow. Chemical Engineering Science 3, 65–73.

Tchen, C., 1947. Mean value and correlation problems connected with the motion of small particles suspended in a turbulent fluid. Ph.D. thesis. Delft.

Tenetti, S., Subramanian, S., 2014. Particle-resolved direct numerical simulation for gas-solid flow model development. Ann. Rev. Fluid Mech. 46, 199–230.

Uhlmann, M., 2005. An immersed boundary method with direct forcing for the simulation of particulate flows. Journal of Computational Physics 209, 448–476.

Uhlmann, M., Dušek, J., 2014. The motion of a single heavy sphere in ambient fluid: A benchmark for interface-resolved particulate flow simulations with significant relative velocities. International Journal of Multiphase Flow 59, 221 – 243.

Vincent, S., Brändle de Motta, J.C., Sarthou, A., Estivalezes, J.L., Simonin, O., Climent, E., 2014. A Lagrangian VOF tensorial penalty method for the DNS of resolved particle-laden flows. Journal of Computational Physics 256, 582–614.

Zhang, K., Guan, Y., Yao, X., Li, Y., Fan, X., Brandani, S., 2013. Two- and three-dimensional computaional studies of liquid-solid fluidization. Powder Technology 235, 180–191.

Zhang, Z., Botto, L., Prosperetti, A., 2006. Microstructural effects in a fully-resolved simulation of 1,024 sedimenting spheres, in: Balachandar, S., Prosperetti, A. (Eds.), IUTAM Symposium on Computational Approaches to Multiphase Flow. Springer Netherlands. number 81 in Fluid Mechanics and Its Applications, pp. 197–206.

Zhang, Z., Prosperetti, A., 2005. A second-order method for three-dimensional particle simulation. Journal of Computational Physics 210, 292–324.